A transferable electrostatic map for solvation effects on amide I vibrations and its application to linear and two-dimensional spectroscopy

Thomas la Cour Jansen and Jasper Knoester

A transferable electrostatic map for solvation effects on amide I vibrations and its application to linear and two-dimensional spectroscopy

Thomas la Cour Jansen[a] and Jasper Knoester
*Institute for Theoretical Physics and Materials Science Centre, University of Groningen, Nijenborgh 4,
9747 AG Groningen, The Netherlands*

A method for modeling infrared solvent shifts using the electrostatic field generated by the solvent is presented. The method is applied to the amide I vibration of N-methyl acetamide. Using *ab initio* calculations the fundamental frequency, anharmonicity, and the transition dipoles between the three lowest vibrational states are parametrized in terms of the electrostatic field. The generated map, which takes into account the electric field and its gradients at four molecular positions, is tested in a number of common solvents. Agreement of solvent shift and linewidths with experimental Fourier transform infrared (FTIR) data is found to be within seven and four wave numbers, respectively, for polar solvents. This shows that in these solvents electrostatic contributions dominate solvation effects and the map is transferable between these types of solvents. The effect of motional narrowing arising from the fast solvent fluctuations is found to be substantial for the FTIR spectra. Also the two-dimensional infrared (2DIR) spectra, simulated using the constructed map, reproduce experimental results very well. The effect of anharmonicity fluctuations on the 2DIR spectra was found to be negligible. © *2006 American Institute of Physics*. [DOI: 10.1063/1.2148409]

I. INTRODUCTION

Infrared spectroscopy of the amide I transition of proteins provides a tool to probe their conformation.[1–3] However, the linear absorption spectrum of this band is in general broad and featureless due to overlapping contributions from inhomogeneous distributions of environments. Two-dimensional infrared (2DIR) spectroscopy has been found to be more sensitive to molecular structure[4–12] due to the fact that this technique spreads the response in two dimensions and allows for the observation of the coupling between the underlying peaks. Moreover, this and related techniques have the ability to probe the dynamics from the millisecond down to a subpicosecond time scale.[13–15]

While the 2DIR spectra have already been measured for several proteins[4,5] and theoretical models have been applied to distinguish between different secondary structures,[5,10,16,17] the connection between the microscopic structural disorder and dynamics and the observed spectra is not well established. In highly ordered structures the vibrational states are delocalized over the entire system due to coupling between neighboring peptide units. Disorder and dynamics arising from side groups and solvent modulate the site frequencies and couplings and tend to localize the vibrational states.

The goal of this paper is to study the solvent effects on the amide I vibration (predominantly CO stretch) of polypeptides. In particular, we aim to establish the effect of the environment on the frequencies of individual oscillators. This will be done using *ab initio* calculations in which the solvent shift is related to the electrostatic field generated by the solvent. The effect on the anharmonicity and transition dipoles of individual oscillators will be examined as well. Thus the

advantage of this method over previous ones is that the generated maps are transferable, i.e., the same map applies to different solvents.

The solvent effects on the frequency, anharmonicity, and transition dipole of a single oscillator can be studied by using N-methyl acetamide (NMA) as a model system for a single peptide unit.[2–4] The amide I mode primarily consists of the CO stretching vibration. In proteins this vibration has a frequency at 1650 cm^{-1} for α helices, while two peaks, occurring around 1640 and 1680 cm^{-1}, are observed for β sheets. These frequencies are in the same range as the water bend mode near 1600 cm^{-1}. Infrared measurements on proteins are therefore commonly performed in heavy water, where the bend vibration is moved to 1200 cm^{-1}. Upon solvation of NMA and proteins in heavy water, the hydrogen bound to the amide nitrogen atom is exchanged with deuterium. The predominant isotopic species of NMA in heavy water is thus the one deuterated on nitrogen (NMA-*d*). The gas-phase frequency of the amide I mode in NMA-*d* is 1717 cm^{-1},[18] and the overtone frequency is 3424 cm^{-1}, corresponding to an anharmonicity of 10 cm^{-1}.

The vibrational frequencies of a molecule are determined by the potential-energy surface (PES) on which its nuclei are moving. The PES depends on the electronic configuration of the solute as well as the forces exerted by the solvent. Because in many solvents the electrostatic forces dominate, one expects that describing the solute in an electrostatic field provides a good approximation of the solvation effects. Formally the PES of a molecule in an inhomogeneous electric field is determined by the electrostatic potential $\phi(\bar{r})$ in the complete surrounding space. However, it is in practice impossible to tabulate the electrostatic potential in every point of space. Instead, if the potential is slowly vary-

a)Electronic mail: thomas.lacour@gmail.com

ing, it is sufficient to know its value in a few points. Alternatively, knowledge of the electric field $\bar{E}(\bar{r}) = -\bar{\nabla}\phi(\bar{r})$ and its gradient tensor $\bar{\bar{G}}(\bar{r}) = \bar{\nabla} \otimes \bar{E}(\bar{r})$ in several points may suffice to characterize the electrostatic fields. This suggests that a map can be constructed for the electrostatic solvent effects on properties such as the vibrational frequencies, transition dipoles, etc., in terms of the electrostatic potential, or the electric field, or the electric field and its gradient at a number of points in the solute molecule. The accuracy of these maps will depend on how well the overall electrostatic potential is reconstructed by the potential, field, and gradients in the given points.

Maps of this type have already been reported in literature. Specifically, several maps were designed for the amide I frequency of NMA-d that depend on the electrostatic potential on four or six atomic sites.[19–22] One map was constructed that uses the electrostatic potential at four atomic sites and three bond positions.[23] Field maps were designed for the same amide I vibration and for the OH and OD vibrations in HOD depending on the electric field on four atoms in NMA-d (Ref. 22) and on all three atoms in HOD.[24] For the OH stretch in HOD a map only depending on the electric-field component on hydrogen directed along the bond has been presented as well.[25] Finally, a map depending on the field and gradients in one point has been presented for HOD in D_2O.[26]

The existing NMA-d maps[19–23] were constructed using ab initio calculations on NMA-d in water clusters. The electrostatic potentials were determined from particular molecular-dynamics (MD) force fields and used to obtain the fit parameters. In this way not only the electrostatic effects were included in the map but also the possible effects arising from dispersion forces, charge transfer, and covalent bonding. While this inclusion might make these maps particularly good for simulations of spectra in water using the same MD force field as used in the fit, this procedure possibly produces artifacts in other environments. In contrast, by using electric fields or point charges in the ab initio calculations, the true electrostatic effect can be isolated. A map based on such a principle will be transferable and can possibly be used to optimize MD force fields to give a better description of the local electrostatic environment, since such map is not optimized to a specific force field. Nonelectrostatic effects such as those arising from dispersion, charge transfer, and covalent bonding will, of course, not be accounted for and have to be treated separately when they give important contributions to the frequency fluctuations. In that case they can then be added safely without the risk of double counting.

The existing maps used the electrostatic potential or electric field for their parametrization. By including electric-field gradients the effect of inhomogeneity in the electrostatic potential can be elucidated. Here we report the construction of a map for the vibrational frequency, anharmonicity, and transition dipole of the amide I vibration in NMA-d using the electric-fields and electric field gradients on four atoms. Applications to Fourier transform infrared (FTIR) and 2DIR spectra of NMA-d in various solvents are discussed as well.
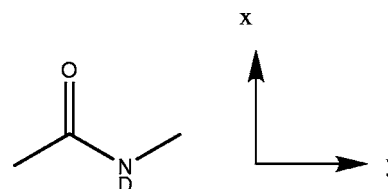
The remainder of this paper is organized as follows. In

FIG. 1. The chemical structure of NMA-d shown in the used coordinate system. The x axis is aligned exactly along the CO bond. The z axis goes into the paper.

Sec. II the construction of the map will be described. The MD simulations and line-shape calculations will be described in Sec. III. The results are discussed in Sec. IV, and finally the conclusions will be drawn in Sec. V.

II. THEORY

We express a molecular quantity Q (such as the fundamental oscillator frequency) in terms of its value in the gas phase, Q_0, a vector containing the electrostatic potential or field parameters $|E\rangle$, and the map vector $|c\rangle$:

$$Q = Q_0 + \langle c|E\rangle. \tag{1}$$

For NMAD-d (Fig. 1) we used the electric field in the x and y directions and the zz and xy gradients on the C, O, N, and D atoms (denoted by E_x^C, etc.) to parametrize the map. For this parameterization the electric-field vector $|E\rangle = (E_x^C, E_y^C, E_{zz}^C, E_{xy}^C, E_x^O, E_y^O, E_{zz}^O, E_{xy}^O, E_x^N, E_y^N, E_{zz}^N, E_{xy}^N, E_x^D, E_y^D, E_{zz}^D, E_{xy}^D)$ and the vector $|c\rangle$ contains the corresponding 16 fit parameters.

Ab initio calculations were performed with the ADF program[27] using the ADF TZ2P basis and the RPBE exchange correlation functional.[28,29] First the geometry of NMA-d was optimized. The Hessian was constructed in the optimized geometry using 0.01 Å distortions of the Cartesian coordinates. This was done by fixing the positions of the methyl groups and varying the position of the carboxyl carbon and oxygen as well as the nitrogen and deuterium. The methyl movement was excluded to assure that the same amide normal mode can be used in later calculations, where the methyl groups are substituted by other groups. This exclusion lowers the amide I frequency by 0.6%. The normal modes for the amide unit of NMA-d were found by diagonalizing the Hessian. The reduced mass M for amide I was found to be 12.858 amu and the gas-phase frequency ω in this harmonic approximation was 1663.53 cm^{-1}.

For the amide I mode a vibrational Hamiltonian beyond the harmonic approximation was constructed as follows: The PES for this mode was obtained by distorting the equilibrium geometry using the amide I normal mode. A total of 11 points on the PES was calculated with 0.06 Å displacement between neighboring points. The PES was expanded in a Taylor series up to sixth order in the amide I coordinate (R),

$$V(R) = V_0 + V_1 R + \frac{1}{2!} V_2 R^2 + \frac{1}{3!} V_3 R^3 + \frac{1}{4!} V_4 R^4 + \frac{1}{5!} V_5 R^5$$

$$+ \frac{1}{6!} V_6 R^6, \tag{2}$$

where the coefficients were obtained using a least-squares fit to the calculated PES. The Hamiltonian for the amide I coordinate,

$$H = \frac{P^2}{2M} + V(R), \tag{3}$$

was quantized by transforming the coordinate R and momentum P to bosonic creation ($B^\dagger$) and annihilation (B) operators corresponding to the harmonic gas-phase normal mode:

$$R = \sqrt{\frac{\hbar}{2M\omega}}(B^\dagger + B),$$

$$P = i\sqrt{\frac{M\omega\hbar}{2}}(B^\dagger - B). \tag{4}$$

The bosonic operators satisfy the Bose commutation relation $[B, B^\dagger] = 1$. The thus obtained vibrational Hamiltonian is given in Eq. (4) of Ref. 30. The Hamiltonian was expanded in the harmonic basis using the 21 lowest basis functions ($\phi_0 - \phi_{20}$), with

$$\phi_n = \frac{1}{\sqrt{n!}}(B^\dagger)^n |0\rangle \tag{5}$$

and $|0\rangle$ denoting the ground state found in the harmonic approximation. The energy and wave functions were found for the three lowest states (g: ground, e: singly excited, and f: doubly excited states) by diagonalizing the Hamiltonian. The transition dipoles were found from the first-order derivative of the dipole moment obtained in the *ab initio* calculation, using the dipole operator

$$\bar{\mu} = \bar{\mu}_0 + \frac{\partial\bar{\mu}}{\partial R}\sqrt{\frac{\hbar}{2M\omega}}(B^\dagger + B). \tag{6}$$

To construct the map Eq. (1), the above calculation was repeated in 74 different point-charge environments, chosen to ensure that the 16 electrostatic field and gradient components used in the map were sampled sufficiently. The fundamental (ω_{eg}) and overtone frequencies (ω_{fg}) as well as the transition dipoles (μ_{ge}, μ_{gf}, and μ_{ef}) were calculated in the same way as for the gas phase. These properties were fitted to the electrostatic field and gradients to yield the 16 coefficients of the vector $|c\rangle$ [Eq. (1)]. The fits were performed both with the least-squares method and the singular value decomposition method[31] to eliminate linear dependencies. Such dependencies would blow up the linearly dependent coefficients in the least-squares method and minimize these coefficients in the singular value decomposition method. For the 74 different point-charge and gas-phase calculations performed, the two fitting methods gave practically identical coefficients.

The gas-phase frequency was found to be 1660.63 cm^{-1}, slightly lower than that obtained in the harmonic approxima-

TABLE I. The frequency map parameters given in cm$^{-1}/(E_h/e$ bohr) for the fields and in cm$^{-1}/(E_h/e$ bohr^2) for the gradients.

Atom	Field	$c(\omega_{ge})$	$c(\omega_{fg})$
	Vacuum	1717	3421.62
C	E_x	2188.0	4399.4
	E_y	171.0	346.4
	E_{zz}	−90.0	−185.0
	E_{xy}	−3953.9	−7988.1
O	E_x	990.0	1970.1
	E_y	898.3	1811.0
	E_{zz}	433.6	867.5
	E_{xy}	−469.4	−945.8
N	E_x	470.3	952.1
	E_y	−805.1	−1428.8
	E_{zz}	−1070.9	−2155.0
	E_{xy}	−4141.1	−8593.1
D	E_x	230.2	454.1
	E_y	−1854.8	−3933.7
	E_{zz}	−454.8	−923.2
	E_{xy}	−2049.4	−4319.4

tion. In order to reproduce the measured gas-phase frequency (1717 cm^{-1}), all frequencies were scaled with an identical scaling factor of 3.395%, assuming (as is common in *ab initio* calculations of vibrational frequencies[32]) that the discrepancy is systematic. After scaling the frequency for the doubly excited state was found to be 3421.62 cm^{-1}, only deviating an additional 0.07% from the experimental value. This gives a calculated anharmonicity ($\Delta = 2\omega_{eg} - \omega_{fg}$) of 12.38 cm^{-1} in the gas phase. For the final map, to be applied in the next sections, we used the least-squares-fit coefficients, all of which are given in Tables I and II. As an indication for the quality of the map, we show in Fig. 2 the correlation between the calculated ($\omega_{eg,\text{DFT}}$) and fitted frequencies ($\omega_{eg,\text{map}}$) for the 75 charge environments considered.

If the dependence of the oscillator frequency (and dipole) on the electric field deviates significantly from a linear relationship such as proposed in Eq. (1), the fit coefficients c will depend on the choice of point-charge environments. One could have chosen these environments by using the point charges from MD simulations of NMA-d in a particular solvent. It is likely that this would give a better map for that solvent. However, such a map could not be expected to perform as well for other solvents, i.e., it would not be transferable. Combining point-charge configurations from different solvents could improve this, but we do not expect that this would lead to considerable differences in the fit coefficients compared to our chosen variety of point charges. If substantial deviations from the linear relationship exist, a transferable map can only be obtained by expanding Eq. (1) to higher orders in the electric field. The neat linear correlation between the DFT frequencies and the map frequencies seen in Fig. 2 indicates that such nonlinearities are of minor importance for the present system.

TABLE II. The dipole map parameters given in D/(E_h/e bohr) for the fields and in D/(E_h/e bohr^2) for the gradients.

Atom	Field	$c(\mu_{ge:x})$	$c(\mu_{ge:y})$	$c(\mu_{ef:x})$	$c(\mu_{ef:y})$	$c(\mu_{gf:x})$	$c(\mu_{gf:y})$
	Vacuum	0.242 141	−0.085 961	0.343 344	−0.121 888	0.012 656	−0.004 493
C	E_x	−0.381	0.296	−0.539	0.419	−0.016 8	0.014 2
	E_y	−0.077	−0.585	−0.109	−0.830	−0.004 4	−0.029 7
	E_{zz}	0.104	0.379	0.148	0.537	0.004 8	0.020 1
	E_{xy}	−0.182	−0.539	−0.253	−0.767	0.004 1	−0.0321
O	E_x	−1.177	0.344	−1.670	0.488	−0.065 8	0.019 6
	E_y	0.119	0.003	0.169	0.004	0.004 1	−0.000 1
	E_{zz}	−0.360	0.146	−0.510	0.207	−0.020 5	0.008 4
	E_{xy}	−0.110	−0.479	−0.156	−0.679	−0.006 3	−0.024 3
N	E_x	−0.087	−0.232	−0.125	−0.329	−0.010 0	−0.010 0
	E_y	0.431	−1.113	0.587	−1.569	−0.011 4	−0.045 2
	E_{zz}	0.081	−0.029	0.115	−0.041	0.006 3	−0.024 3
	E_{xy}	0.618	1.670	0.909	2.356	0.088 5	0.065 9
D	E_x	−0.045	0.183	−0.063	0.259	0.000 7	0.008 4
	E_y	0.061	1.168	0.112	1.646	0.042 2	0.046 1
	E_{zz}	−0.181	−0.017	−0.256	−0.024	−0.009 7	−0.000 7
	E_{xy}	−0.143	1.249	−0.178	1.762	0.029 6	0.051 1

III. SIMULATION

The electrostatic map was tested for NMA-d in a range of solvents using MD simulations. All simulations were performed with the GROMOS87 force field[33–35] for NMA-d using the GROMACS MD package.[36] The calculations were done in the *NPT* ensemble at 300 K and 1 bar.[37,38] Periodic boundary conditions were applied and cutoffs in the interactions at half the box size were used to avoid interactions with the self-images.[38] The Lennard-Jones force fields for solvent-solute interactions were constructed using the geometric combination rule.[39] NMA-d was simulated in the following five solvents: heavy water (D_2O), methanol-d (MeOD), acetonitrile (MeCN), dimethyl sulfoxide-d_6 (DMSO-d_6), and chloroform-d (CDCl$_3$). All solvent molecules were kept rigid using the SHAKE (Ref. 40) (DMSO-d_6 and CDCl$_3$) or LINCS (Ref. 41) (D_2O, MeOD, and MeCN) algorithms. MeOD was simulated for 5 ns and D_2O was simulated for 4 ns, while the other solvents were simulated for 1 ns. The frequencies, dipoles, and anharmonicities were obtained every 10 fs. The long simulation times for MeOD and D_2O were needed because these solvents form strong slowly exchanging hydrogen bond complexes with NMA-d.

In the case of heavy water, 346 D_2O molecules were described with the extended simple point charge (SPC/E) force field.[42] For MeOD the GROMOS Lennard-Jones force field[33–35] was combined with the methanol charges from AMBER (q_O=−0.6497 e, q_{CH_3}=0.2282 e, and q_D=0.4215 e), identical to the charges used in an earlier study of NMA-d in methanol;[43] 395 MeOD molecules were used. A united atom model[44] was used to simulate 188 MeCN molecules. For the 206 molecule DMSO-d_6 solution, the GROMOS force field[33–35] was used. Finally, the 158 CDCl$_3$ molecules were treated with the OPLS force field.[45]

A. Calculation of spectra

The FTIR and 2DIR spectra were simulated assuming an adiabatic approximation for the time evolution.[46] The linear absorption (FTIR) was calculated in the time domain using the response function

$$S^{(1)}(\tau_1 - \tau_0) = \frac{i}{\hbar}\mu_{ge}(\tau_1)U_{eg}(\tau_1,\tau_0)\mu_{ge}(\tau_0)$$

$$\times \exp(-(\tau_1 - \tau_0)/2T_1) + \text{c.c.} \tag{7}$$

The transition dipole for the excitation from the ground state to the excited state $\mu_{ge}(t)$ is obtained from the map and is rotated from the molecular frame to the simulation box frame using the configuration at time t. T_1 is the lifetime of the excited state, accounted for in this *ad hoc* approximation,[43,47] and is assumed to be 1.8 ps in all simulations.[47] The general time evolution $U_{ab}(t)$ is determined by the map frequency ω_{ab},
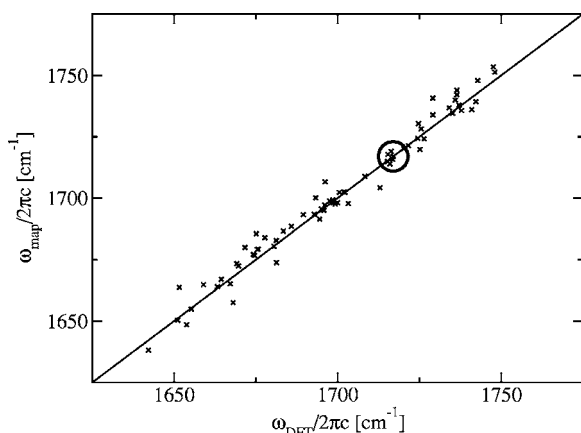

FIG. 2. Correlation plot between the (scaled) *ab initio* frequencies and the map frequencies for the 75 charge environments considered in this paper. The circle denotes the gas-phase case.

$$U_{ab}(\tau_1, \tau_0) = \exp\left(-\frac{i}{\hbar}\int_{\tau_0}^{\tau_1}\omega_{ab}(\tau)d\tau\right). \tag{8}$$

For the linear absorption only the time evolution involving the fundamental frequency ω_{eg} is needed. The time domain response function was calculated by averaging over each trajectory using 200 fs between sample points for τ_0. The frequency domain absorption spectra were calculated as the Fourier transform of the time domain response functions.

2DIR spectroscopy is a four-wave-mixing technique.[4,48] The 2DIR spectra are given as the sum of the signal emitted in the directions with wave vectors $\bar{k}_I = -\bar{k}_1 + \bar{k}_2 + \bar{k}_3$ and $\bar{k}_{II} = \bar{k}_1 - \bar{k}_2 + \bar{k}_3$, where $\bar{k}_1$, $\bar{k}_2$, and $\bar{k}_3$ are the wave vectors of the incoming infrared fields. $\bar{k}_I$ is the photon-echo signal and $\bar{k}_{II}$ is the nonrephasing signal. Each of these signals contains three contributions from three distinct Liouville space pathways: ground-state bleach (GB), stimulated emission (SE), and excited-state absorption (EA).[43,49] These are given by

$$S_{GB}^{(I)}(\tau_3 - \tau_2, \tau_2 - \tau_1, \tau_1 - \tau_0)$$
$$= -\left(\frac{i}{\hbar}\right)^3 \mu_{ge}(\tau_3)\mu_{ge}(\tau_2)\mu_{ge}(\tau_1)u_{ge}(\tau_0)U_{eg}(\tau_3, \tau_2)$$
$$\times U_{gg}(\tau_2, \tau_1)U_{ge}(\tau_1, \tau_0)$$
$$\times \exp(-(\tau_3 - \tau_0 + \tau_2 - \tau_1)/2T_1), \tag{9}$$

$$S_{GB}^{(II)}(\tau_3 - \tau_2, \tau_2 - \tau_1, \tau_1 - \tau_0)$$
$$= -\left(\frac{i}{\hbar}\right)^3 \mu_{ge}(\tau_3)\mu_{ge}(\tau_2)\mu_{ge}(\tau_1)u_{ge}(\tau_0)U_{eg}(\tau_3, \tau_2)$$
$$\times U_{gg}(\tau_2, \tau_1)U_{eg}(\tau_1, \tau_0)$$
$$\times \exp(-(\tau_3 - \tau_0 + \tau_2 - \tau_1)/2T_1), \tag{10}$$

$$S_{SE}^{(I)}(\tau_3 - \tau_2, \tau_2 - \tau_1, \tau_1 - \tau_0)$$
$$= -\left(\frac{i}{\hbar}\right)^3 \mu_{ge}(\tau_3)\mu_{ge}(\tau_2)\mu_{ge}(\tau_1)u_{ge}(\tau_0)U_{eg}(\tau_3, \tau_2)$$
$$\times U_{ee}(\tau_2, \tau_1)U_{ge}(\tau_1, \tau_0)$$
$$\times \exp(-(\tau_3 - \tau_0 + \tau_2 - \tau_1)/2T_1), \tag{11}$$

$$S_{SE}^{(II)}(\tau_3 - \tau_2, \tau_2 - \tau_1, \tau_1 - \tau_0)$$
$$= -\left(\frac{i}{\hbar}\right)^3 \mu_{ge}(\tau_3)\mu_{ge}(\tau_2)\mu_{ge}(\tau_1)u_{ge}(\tau_0)U_{eg}(\tau_3, \tau_2)$$
$$\times U_{ee}(\tau_2, \tau_1)U_{eg}(\tau_1, \tau_0)$$
$$\times \exp(-(\tau_3 - \tau_0 + \tau_2 - \tau_1)/2T_1), \tag{12}$$

$$S_{EA}^{(I)}(\tau_3 - \tau_2, \tau_2 - \tau_1, \tau_1 - \tau_0)$$
$$= \left(\frac{i}{\hbar}\right)^3 \mu_{fe}(\tau_3)\mu_{fe}(\tau_2)\mu_{ge}(\tau_1)\mu_{ge}(\tau_0)U_{fe}(\tau_3, \tau_2)$$
$$\times U_{ee}(\tau_2, \tau_1)U_{ge}(\tau_1, \tau_0)$$
$$\times \exp(-(\tau_3 - \tau_0 + \tau_2 - \tau_1)/2T_1 - (\tau_3 - \tau_2)/2T_2), \tag{13}$$

$$S_{EA}^{(II)}(\tau_3 - \tau_2, \tau_2 - \tau_1, \tau_1 - \tau_0)$$
$$= \left(\frac{i}{\hbar}\right)^3 \mu_{fe}(\tau_3)\mu_{fe}(\tau_2)\mu_{ge}(\tau_1)\mu_{ge}(\tau_0)U_{fe}(\tau_3, \tau_2)$$
$$\times U_{ee}(\tau_2, \tau_1)U_{eg}(\tau_1, \tau_0)$$
$$\times \exp(-(\tau_3 - \tau_0 + \tau_2 - \tau_1)/2T_1 - (\tau_3 - \tau_2)/2T_2). \tag{14}$$

Here, $\tau_0 - \tau_2$ are the times at which the molecule interact with the incoming infrared fields, and τ_3 is the (heterodyne) detection time, $\tau_3 \geq \tau_2 \geq \tau_1 \geq \tau_0$. In the present simulations the second time interval was fixed at zero, $t_2 = \tau_2 - \tau_1 = 0$. The lifetime of the overtone T_2 was set to be $T_1/2$.[43] The signals were converted to the frequency domain using two-dimensional (2D) Fourier transforms of the time differences $t_1 = \tau_1 - \tau_0$ and $t_3 = \tau_3 - \tau_2$:

$$S^{(I)}(\omega_3, t_2, \omega_1) = \int_0^\infty \int_0^\infty (S_{GB}^{(I)}(t_3, t_2, t_1)$$
$$+ S_{SE}^{(I)}(t_3, t_2, t_1) + S_{EA}^{(I)}(t_3, t_2, t_1))$$
$$\times \exp(i(\omega_3 t_3 - \omega_1 t_1))dt_3 dt_1,$$

$$S^{(II)}(\omega_3, t_2, \omega_1) = \int_0^\infty \int_0^\infty (S_{GB}^{(II)}(t_3, t_2, t_1) + S_{SE}^{(II)}(t_3, t_2, t_1)$$
$$+ S_{EA}^{(II)}(t_3, t_2, t_1))\exp(i(\omega_3 t_3 + \omega_1 t_1))dt_3 dt_1. \tag{15}$$

Finally, the 2DIR spectrum is the imaginary part of the sum of the photon-echo and nonrephasing signals,

$$I_{2D}(\omega_3, t_2, \omega_1) = \mathrm{Im}(S^{(I)}(\omega_3, t_2, \omega_1) + S^{(II)}(\omega_3, t_2, \omega_1)). \tag{16}$$

All spectra were calculated for parallel polarized ($zzzz$) laser fields as used for the experiments in Ref. 15.

IV. RESULTS AND DISCUSSION

A. Linear spectra

The simulated linear absorption spectra are shown in Fig. 3 (dashed), together with the measured spectra (solid) and the simulated frequency distribution (dotted). The peak positions are given in Table III, along with the deviation between the simulations and experiment, while the full width at half maximum (FWHM) linewidths (Γ) are given in Table IV. For MeOD the linewidths were determined using Gaussian fits to the two-peak line shape; since the two peaks overlap and are not necessarily Gaussian, the accuracy of both linewidths should be taken with caution. The static linewidth (Γ_{static}) is the FWHM of the distribution of instantaneous frequencies. The line-broadening parameter κ is defined as the ratio between the frequency fluctuation relaxation rate and the standard deviation of these fluctuations[49] for the Gaussian Markovian fluctuations. It is related to the ratio between the actual linewidth and the width of the frequency distribution and can be estimated from the ratio Γ/Γ_{static} utilizing the Padé approximant.[49] In the homogeneous limit the actual linewidth is much narrower than the frequency distribution and κ goes to infinity. In the inhomogeneous limit the actual linewidth is the same as that of the frequency distri-
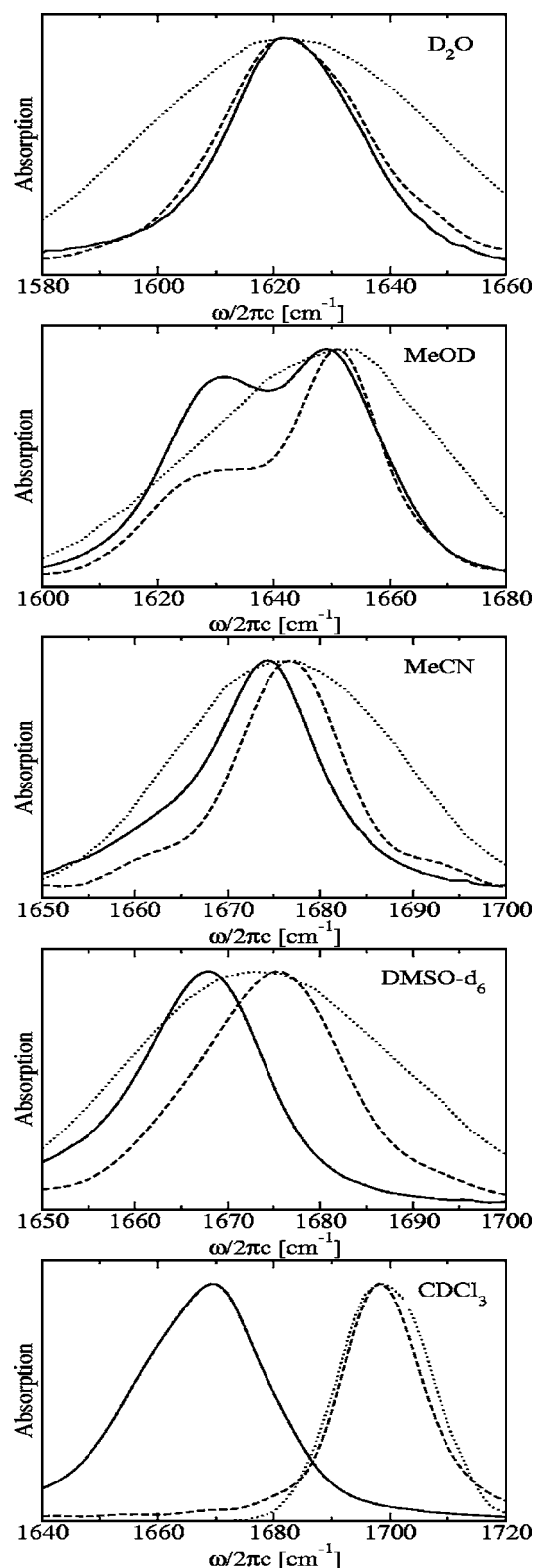
FIG. 3. The linear absorption spectrum of NMA-d in various solvents. Full line: experiment, dotted line: simulated frequency distribution, and dashed line: simulated spectrum. All spectra are normalized to the same peak height. Experimental data are from Ref. 15.

bution and κ goes to zero. The line-broadening parameters were estimated from the ratio between the simulated dynamic (Γ) and static (Γ_{static}) linewidths.[49]

As seen from Table III for the majority of the solvents, the simulated amide I frequencies in solution are deviating

TABLE III. FTIR peak frequencies (in cm^{-1}) in different solvents, as obtained from our simulations and from experiment (Ref. 15). The last column gives the discrepancies.

Solvent	Simulated	Experimental	Difference
D$_2$O	1622	1622	0
MeOD[a]	1628	1631	−3
MeOD[b]	1652	1649	3
MeCN	1677	1674	3
DMSO-d_6	1675	1668	7
CDCl$_3$	1698	1669	29

[a]The low-frequency peak.
[b]The high-frequency peak.

less than 10 cm^{-1} from the experimental values (in water the deviation is practically zero). This indicates that the majority of the solvent shift in these solvents is of electrostatic origin. Table IV shows that the linewidths Γ are also described very well by our simulations, with typical deviations from experiment within 3–4 cm^{-1} (10%–15%). Motional narrowing is found to play an important role in all the solutions, reducing the dynamic linewidth to half of the value predicted by the static distribution. In all solvents the line-broadening parameter is in the intermediate regime ($\kappa \approx 1$), implying that the line shape is neither well represented by a Gaussian nor a Lorentzian.

In MeOD the experimentally observed two-peak structure is recovered in the simulated spectrum. This structure is due to the existence of two different hydrogen bond species.[50] As we see, the low-frequency species is underrepresented in the simulated spectrum, which is due to an error in the free energy difference between the two species predicted by the force field. The error can be estimated from the ratios between the populations in the simulation and the experiment and a rough estimate from the peak intensity (I) gives an error in the order of $\Delta G = RT \ln((I^1_{sim}/I^2_{sim})/(I^1_{exp}/I^2_{exp})) \sim 2$ kJ/mol.

In one solvent a clear breakdown of the electrostatic map is observed. In CDCl$_3$ the predicted frequency is 29 cm^{-1} off and the predicted linewidth is 10 cm^{-1} too narrow. In CDCl$_3$ the Coulomb interaction is much weaker than in the other solutions, and the dispersion forces originating from the big chlorine atoms dominate. In Table V the simulated Coulomb and Lennard-Jones energies are given along with the ratio

TABLE IV. FTIR line-shape parameters in different solvents. Γ, Γ_{static}, and Γ_{expt} denote, respectively, the FWHM (in cm^{-1}) of the simulated spectrum, the simulated static distribution of frequencies, and the experimental spectrum (Ref. 15); κ is the estimated line-broadening parameter. All units are in cm^{-1}.

Solvent	Γ_{expt}	Γ	Γ_{static}	Γ/Γ_{static}	κ
D$_2$O	27.8	30.8	59.6	30.8	0.517
MeOD[a]	~27	25.3	35.5	0.712	0.80
MeOD[b]	~23	19.7	44.7	0.441	1.8
MeCN	14.6	13.7	28.3	0.484	1.6
DMSO-d_6	16.2	19.3	35.0	0.551	1.3
CDCl$_3$	26.7	16.4	19.1	0.858	0.45

[a]The low-frequency peak.
[b]The high-frequency peak.

TABLE V. MD Lennard-Jones (E_{LJ}) and Coulomb (E_C) potential energies (in kcal/mol) and the ratio between them.

Solvent	E_{LJ}	E_C	E_{LJ}/E_C
D_2O	3188.35	−19 499.6	−0.16
MeOD	−1522.83	−12 383.2	0.12
MeCN	−2482.47	−2 927.33	0.85
DMSO-d_6	−6477.14	−4 482.94	1.44
$CDCl_3$	−3462.76	−114.339	30.3

between them. For $CDCl_3$ this ratio is more than one order of magnitude bigger than for the other solvents, showing a solvent highly dominated by the dispersion forces. In order to get a reasonable description of the solvent effects in $CDCl_3$ these forces cannot be neglected. In solvents with strong dispersion forces one might want to employ model types suggested earlier[25,51–54] or possibly add the dispersion forces to the present map by using one of these perturbative schemes for the contribution of the dispersion forces to the frequency shift.

The remaining minor deviations between simulation and experiment can be attributed to inaccuracies in the map due to the approximations inherent to the *ab initio* calculations used, the neglect of higher order inhomogeneity, and the use of traditional (Lennard-Jones and fixed point charge) MD force fields to describe the dynamics and the electric field acting on the solute. While it is, in principle, possible to employ existing methods to improve the accuracy, these are in general computationally too demanding to be practically applicable at present.

B. Frequency correlation functions

The normalized time correlation functions for the simulated frequency fluctuations are shown in Fig. 4. The correlation functions for $CDCl_3$ and MeOD both decay much slower than the correlation functions for the other solvents. The slowly decaying tail in the MeOD correlation function is due to the existence of the two hydrogen bond species that interchange on a time scale much slower than that of translational and librational motions. For $CDCl_3$ the slow time scale is probably due to the slow reorientational time of $CDCl_3$ arising from its large moments of inertia. These time
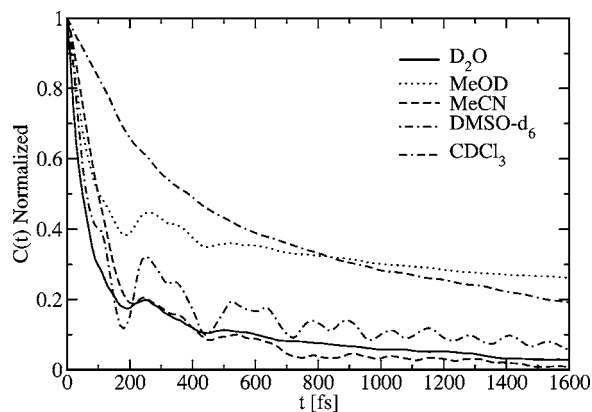

FIG. 4. The simulated frequency correlation functions in the different solvents.

scale differences are in good agreement with those observed for correlation functions extracted from three-pulse photon-echo experiments.[15] In all solvents but $CDCl_3$, oscillations are observed in the correlation functions. These oscillations are most pronounced in DMSO-d_6. All correlation functions could be fitted to a sum of a biexponential function and two underdamped Brownian oscillator functions. Each under-damped Brownian oscillator function is[49]

$$f(t) = \left(\cos(\eta t) + \left(\frac{\gamma}{2\eta} \right) \sin(\eta t) \right) \exp(-\gamma t/2), \qquad (17)$$

where η is the Brownian oscillator frequency and γ is the damping coefficient. The frequencies found in DMSO-d_6 are 113 and 261 cm^{-1}; those in the other solvents have very similar values, indicating that a similar motion is responsible for the oscillations. Since DMSO-d_6 cannot form hydrogen bonds with the NMA-d oxygen, those oscillations cannot be interpreted as hydrogen bond vibrations of the hydrogen bond on the NMA-d oxygen. $CDCl_3$ does not exhibit these oscillations and the $CDCl_3$ cannot form hydrogen bonds with the deuterium atom while all the other solvent molecules can. This leaves oscillations in the hydrogen bond to the NMA-d deuterium open as a possible explanation. These oscillations were not observed in the correlation functions fitted to the experimental three pulse photon echoes,[15] which suggests that the present map overestimates the intensity of these oscillations.

C. Anharmonicity fluctuations

In Fig. 5 the correlation plot between the anharmonicity and the fundamental frequency is shown for 10 000 snapshots of D_2O and MeOD. The correlation coefficients are −0.5849 (D_2O), and −0.8006 (MeOD). The calculated average anharmonicities shown in Table VI are a few wave numbers short of the value of 16 cm^{-1} generally used for 2DIR simulations. That value was determined from the early 2DIR spectrum of NMA-d in DMSO-d_6 experiment,[4] for which a value of 12.6 cm^{-1} was found in the present simulation. In contrast to the gas-phase anharmonicity, which was overestimated by 2.38 cm^{-1} in our simulations, the solvated value is too low. The deviation can arise from the same factors giving rise to the deviations of the fundamental frequency. However, there is the additional possibility that mode mixing between the amide I overtone and, for example, the amide A (NH stretch) vibration plays an important role. Since all modes other than the amide I vibration were fixed in the construction of the vibrational Hamiltonian, such mode mixing was neglected. While including other modes is computationally demanding, it might improve the computed anharmonicity. Furthermore, it should be realized that the experimental uncertainty in the anharmonicity is probably in the order of 1 cm^{-1}.

The standard deviation for the fluctuation of the anharmonicity σ_Δ tabulated in Table VI is varying with almost one order of magnitude between $CDCl_3$ and D_2O. At the end of this section, we will show that this fluctuation hardly has any effect on the 2DIR spectrum and, although the significant difference between the different solvents could have interest-
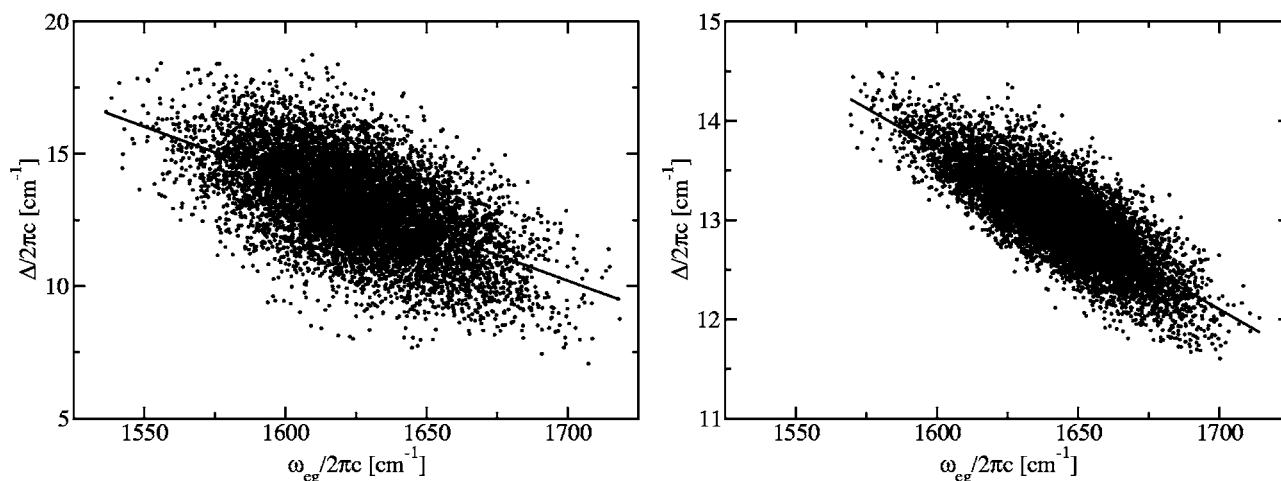
FIG. 5. The correlation between the simulated anharmonicity and the simulated fundamental frequency. Left: D_2O. Right: MeOD. The points for the black scatter plot are taken from 10 ps of the MD simulations. The straight lines are linear fits.

ing implications, this will most likely be undetectable in experiment. With the exception of MeOD there seems to be a correlation between the standard deviation of the frequency $\sigma_{\omega_{eg}}$ and that of the anharmonicity σ_Δ.

D. Transition dipoles

From our simulations, the gas-phase transition dipole for the fundamental excitation turned out to have a magnitude of 0.2569 D and to make an angle of 19.55° with the CO bond. Solvated in water the average magnitude is increased to 0.3137 D, while the average angle is 19.54°. A correlation plot for the x and y components is shown in Fig. 6. The correlation between the two components is rather low with a correlation coefficient of −0.4047. A magnitude of 0.348 D and an angle of 20° have been reported from fitting the transition dipole coupling to experiment in protein structures.[2]

E. 2DIR spectra

The simulated and experimental[15] 2DIR spectra are compared in Fig. 7. While the intensity of the low-frequency peak of MeOD is again underestimated in the simulation and the $CDCl_3$ peaks are too high in frequency and are not broad enough, the remaining experimental spectral features are well recovered in the simulation. This shows that not only the solvent shift and frequency distributions are well described by the map, but that the spectral dynamics, which 2DIR is very sensitive to, is also well described. The simulations well capture the quite different experimental line

shapes of MeCN, DMSO-d_6, and D_2O, going from the round Lorentzian-type shape in MeCN to the shape stretched more along the diagonal in DMSO-d_6 and D_2O. The difference in the estimated κ for these systems is rather small, while the line shapes are significantly different. This is because the correlation functions are not single exponentials and the frequency fluctuations are therefore not Markovian. As a result, the line shapes are not well described by the simple Gaussian Markovian line-broadening theory.

F. Effects of field inhomogeneity

In order to examine the effect of the inhomogeneity in the electric field, three additional maps were constructed using as basis the same 75 *ab initio* calculations as were considered for the full map. In the first map the electrostatic potentials at C, O, N, and D are used. In the next map the electric fields (E_x and E_y) and the gradients (G_{zz} and G_{xy}) in one point (the C atom) are used. For the last map the electric fields on C, O, N, and D are used. These three maps were applied to NMA-d in D_2O, along with the full gradient map.
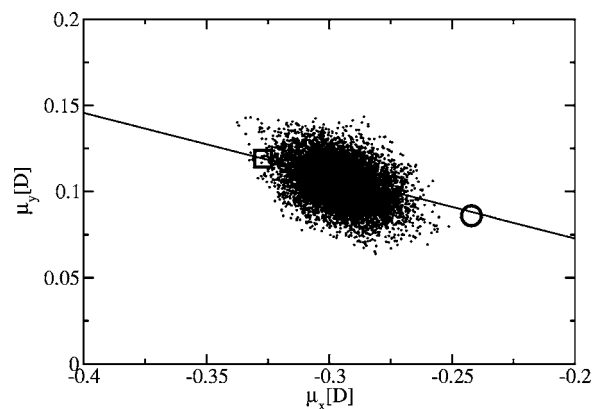
TABLE VI. Mean value and standard deviation of the fundamental frequency (ω_{eg}) and the anharmonicity (Δ) obtained from simulating NMA-d in different solvents. All units are in cm^{-1}.

Solvent	$\langle \omega_{eg} \rangle$	$\sigma_{\omega_{eg}}$	$\langle \Delta \rangle$	σ_Δ
D_2O	1624.2	25.3	13.2	1.7
MeOD	1646.5	21.8	13.0	0.4
MeCN	1676.5	11.7	12.6	0.7
DMSO-d_6	1674.5	14.5	12.6	1.1
$CDCl_3$	1699.3	7.8	12.6	0.2

FIG. 6. The simulated distribution of the transition dipole moment in D_2O solution. The black dots are a scatter plot of the x and y components of the transition dipole moment. The circle indicates the calculated gas phase value, the box denotes the value reported by Krimm and Bandekar (Ref. 2), and the black line represents an angle of 20° between the transition dipole and the CO bond.

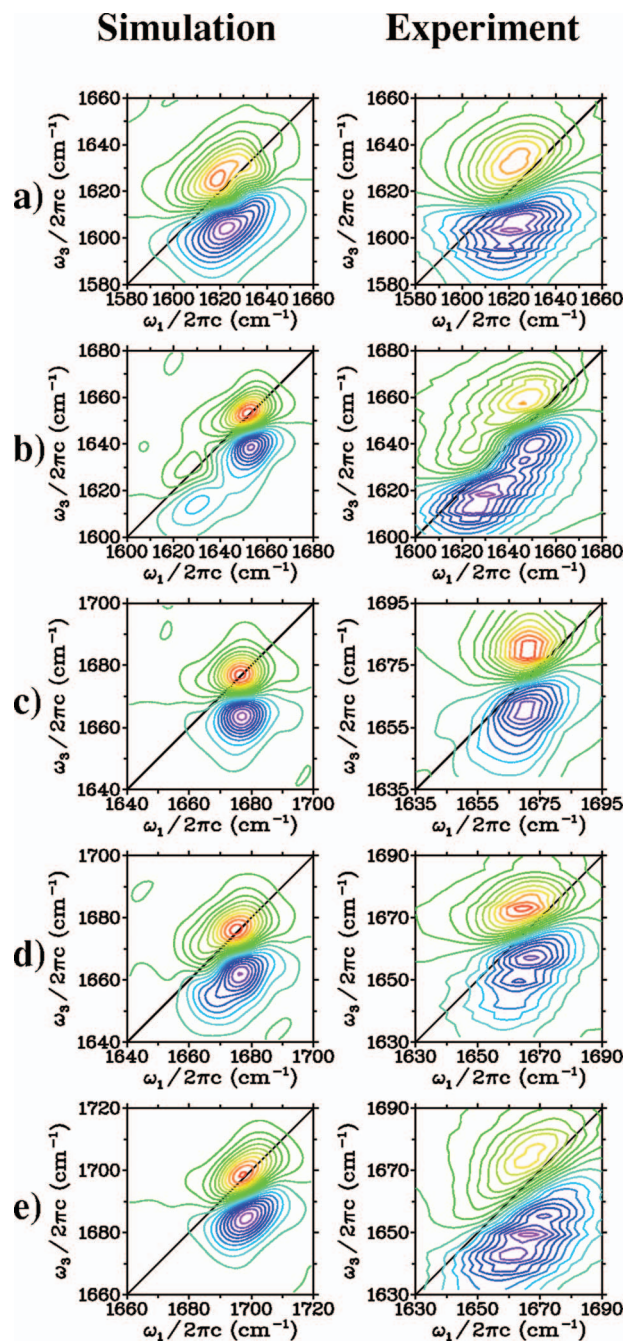## Simulation   ## Experiment

FIG. 7. (Color) 2DIR spectra of NMA-*d* in different solvents. The simulated spectra are shown next to the experimental spectra. (a) D_2O, (b) MeOD, (c) MeCN, (d) DMSO-d_6, and (e) $CDCl_3$. The plots are made with equidistant contours. The green-yellow-red contours are used for negative values (bleaching) and the blue-purple contours are used for positive values (absorption). The experimental data are from Ref. 15.

The linear absorption spectra are shown in Fig. 8, while the corresponding average frequencies, standard deviations, and linewidths are given in Table VII. As we observed above already, the full gradient map very well reproduces the experimental spectrum. By contrast, the potential and field maps give too low frequencies and the point map gives a too high frequency. Furthermore, the linewidth in the potential map is about 75% of that observed for the other maps, which seems to find its origin in the fact that the width of the static distribution is 65% of that of the other maps.
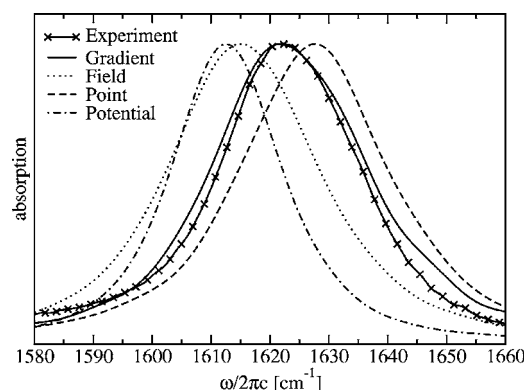

FIG. 8. The linear absorption spectra of NMA-*d* in D_2O calculated with different map types. The experimental data are from Ref. 15.

The frequency time correlation functions according to the four different maps are shown in Fig. 9. The potential map gives a slower decay than the remaining maps. The point map initially decays slower than the field and gradient maps but catches up with those after about 400 fs. Whereas the correlation functions for the potential and point maps are smooth, oscillations are observed in the field and gradient map correlation functions. The field map correlation function oscillation has a higher frequency than the gradient map correlation oscillations that were discussed in more detail earlier in this section. The slower decay of the potential map might be related to the fact that the potential has a $1/r$ dependence and is therefore more sensitive to global dynamics than the field with its $1/r^2$ dependence. Global dynamics is usually slower than local dynamics, thus explaining why the correlation function for the potential map decays slower. If the potential in more closely separated points was used, contributions from neighboring points would cancel for solvent molecules at large distances.

Finally, Fig. 10 presents the 2DIR obtained from different maps [(a)–(e)], as well as from experiment (f). The potential map spectrum (a) is clearly narrower than the remaining spectra, in agreement with the above observation. The field map spectrum (c) is slightly narrower than the point (b) and gradient (d) maps that both describe the experimental line shape (f) very well. The gradient map used for the calculations in the different solvents perform best overall, also predicting the correct solvent shift.

Figure 10(e) presents the 2DIR spectrum of NMA-*d* in D_2O calculated using the full gradient map for the fundamental frequency and dipole μ_{eg} but fixing the anharmonicity at the gas-phase value and scaling the overtone transition dipole according to the harmonic rule $\mu_{fe} = \sqrt{2}\mu_{eg}$. Hardly

TABLE VII. The standard deviation of the fundamental frequency and the calculated FWHM linewidth for NMA-*d* in D_2O obtained with different maps. All units are in cm^{-1}.

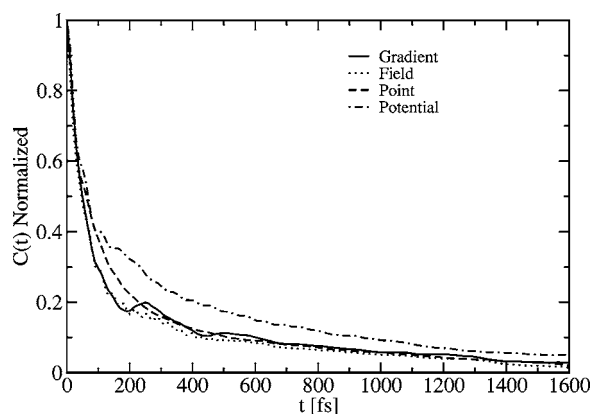| Map	$\langle \omega_{eg} \rangle$	$\sigma_{\omega_{eg}}$	Γ
Potential	1613.4	16.8	22.0
Point	1628.1	23.7	29.5
Field	1616.0	25.5	30.0
Full	1624.2	25.3	30.8

FIG. 9. The frequency correlation function in D_2O for different map types.

any difference is observed between this spectrum (e) and the spectrum (d) that includes the anharmonicity fluctuations and an independent overtone transition dipole. This shows that, at least for a single peptide unit, the approximation with a fixed anharmonicity and a harmonic approximation for the overtone dipole used in the previous studies are sufficient to calculate the 2DIR spectrum.

V. CONCLUSIONS

In this paper we constructed an electrostatic map which quantitatively establishes the effect of the electrostatic potential exerted by a solvent on the vibrational frequency, anharmonicity, and transition dipole of the amide I mode in NMA-d. The map was shown to work very well in polar solvents ranging from dimethyl sulfoxide to water. In chloroform,

where dispersion forces strongly dominate, the map could not predict the correct frequency. An important advantage of our methodology is that a map accounting for the electrostatic solvent effects separately makes it transferable; if needed dispersion force effects can be added without the risk of double counting.

The solvent shifts and linewidths were very well described with the electrostatic map. The static distribution of frequencies was much broader than the actual linewidth, due to motional narrowing. The motional narrowing is caused by the fast fluctuations of the instantaneous frequencies as observed in the correlation functions. For water the correlation functions were compared using different types of maps. The potential map was found to have too slow dynamics to give the correct motional narrowing effect. Small oscillations were observed in the correlation function for the gradient map used in the remaining simulations. Although these oscillations were not observed in echo experiments that probe the correlation function, the overall relaxation time scales found by us does agree with those experiments.

The 2DIR spectrum in three of the five solvents was described very well with the map. For MeOD the discrepancies could be attributed to the failure of the force field combination to give the right free-energy difference between the two hydrogen bond complexes. In $CDCl_3$ the discrepancy was due to the neglect of dispersion interaction effects in our map. We found that, while the fluctuations of the frequencies are important, the fluctuations of the anharmonicity hardly affect the 2DIR spectrum. The same holds for the anharmonic fluctuations of the overtone dipole.

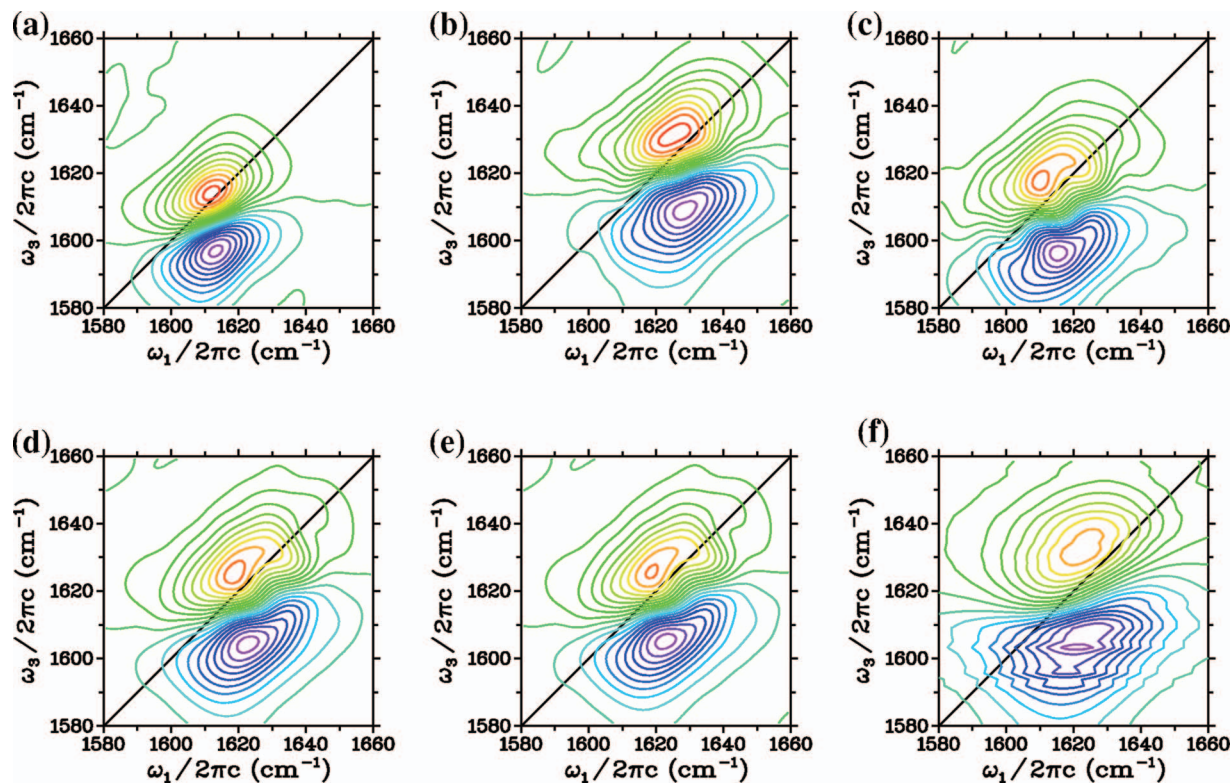The very good description of the frequency fluctuations

FIG. 10. (Color) Simulated 2DIR spectra of NMA-d in D_2O using different maps. (a) Potential, (b) point, (c) field, (d) gradient, (e) gradient with fixed anharmonicity and harmonic approximation for the overtone dipole, and (f) experiment. The color coding is the same as in Fig. 7.

shown by the present pure electrostatic map shows that in polar solvents the solvent effects are dominated by the electrostatic effect. For solvents where the dispersion forces dominate, these forces must be accounted for separately in order to get reasonable frequencies. In peptides and proteins the amide units are in most cases hydrogen bound to other amide units, as seen in helices and sheets, or to solvent water. While aromatic rings and sulfur atoms, giving rise to larger dispersion forces, are present in proteins they are seldom in the very close vicinity of the amide units and since the dispersion forces are of short range, their effect on the amide I frequencies are likely to be small. Therefore, when calculating the amide I site frequencies in proteins, the dispersion forces probably can be safely neglected.

ACKNOWLEDGMENTS

[1] A. Barth and C. Zscherp, Q. Rev. Biophys. **35**, 369 (2002).

[2] S. Krimm and J. Bandekar, Adv. Protein Chem. **38**, 181 (1986).

[3] H. Torii and M. Tasumi, J. Chem. Phys. **96**, 3379 (1992).

[4] P. Hamm, M. H. Lim, and R. M. Hochstrasser, J. Phys. Chem. B **102**, 6123 (1998).

[5] N. Demirdöven, C. M. Cheatum, H. S. Chung, M. Khalil, J. Knoester, and A. Tokmakoff, J. Am. Chem. Soc. **126**, 7981 (2004).

[6] J. H. Choi, S. Ham, and M. Cho, J. Chem. Phys. **117**, 6821 (2002).

[7] M. T. Zanni, S. Gnanakaran, J. Stenger, and R. M. Hochstrasser, J. Phys. Chem. B **105**, 6520 (2001).

[8] S. Woutersen and P. Hamm, J. Chem. Phys. **115**, 7737 (2001).

[9] J. Bredenbeck and P. Hamm, J. Chem. Phys. **119**, 1569 (2003).

[10] C. M. Cheatum, A. Tokmakoff, and J. Knoester, J. Chem. Phys. **120**, 8201 (2004).

[11] A. G. Dijkstra and J. Knoester, J. Phys. Chem. B **109**, 9787 (2005).

[12] S. Woutersen and P. Hamm, J. Chem. Phys. **114**, 2727 (2001).

[13] J. Bredenbeck, J. Helbing, A. Sieg, T. Schrader, W. Zinth, C. Renner, R. Behrendt, L. Moroder, J. Wachtveit, and P. Hamm, Proc. Natl. Acad. Sci. U.S.A. **100**, 6452 (2003).

[14] H. S. Chung, M. Khalil, A. W. Smith, Z. Ganim, and A. Tokmakoff, Proc. Natl. Acad. Sci. U.S.A. **102**, 612 (2005).

[15] M. F. DeCamp, L. DeFlores, J. M. McCracken, A. Tokmakoff, K. Kwac, and M. Cho, J. Phys. Chem. B **109**, 11016 (2005).

[16] D. Abramavicius, W. Zhuang, and S. Mukamel, J. Phys. Chem. B **108**, 18034 (2004).

[17] R. D. Gorbunov, D. S. Kosov, and G. Stock, J. Chem. Phys. **122**, 224904 (2005).

[18] L. C. Mayne and B. Hudson, J. Phys. Chem. **95**, 2962 (1991).

[19] S. Ham, J. H. Kim, H. Lee, and M. H. Cho, J. Chem. Phys. **118**, 3491 (2003).

[20] J. H. Choi, S. Y. Ham, and M. Cho, J. Phys. Chem. B **107**, 9132 (2003).

[21] P. Bour and T. A. Keiderling, J. Chem. Phys. **119**, 11253 (2003).

[22] J. R. Schmidt, S. A. Corcelli, and J. L. Skinner, J. Chem. Phys. **121**, 8887 (2004).

[23] T. M. Watson and J. D. Hirst, Mol. Phys. **103**, 1531 (2005).

[24] S. A. Corcelli, C. P. Lawrence, and J. L. Skinner, J. Chem. Phys. **120**, 8107 (2004).

[25] C. J. Fecko, J. D. Eaves, J. J. Loparo, A. Tokmakoff, and P. L. Geissler, Science **301**, 1698 (2003).

[26] T. Hayashi, T. l. C. Jansen, W. Zhuang, and S. Mukamel, J. Phys. Chem. A **109**, 64 (2005).

[27] C. F. Guerra, O. Visser, J. G. Snijders, G. t. Velde, and E. J. Baerends, in *Methods and Techniques in Computational Chemistry, METECC-5*, edited by E. Clementi and G. Corongiu (STEF, Cagliari, Italy, 1995).

[28] J. P. Perdew, K. Burke, and M. Ernzerhof, Phys. Rev. Lett. **77**, 3865 (1996).

[29] B. Hammer, L. B. Hansen, and J. K. Norskov, Phys. Rev. B **59**, 7413 (1999).

[30] J. Dreyer, J. Chem. Phys. **122**, 184306 (2005).

[31] W. H. Press, S. A. Teukolsky, W. T. Vetterling, and B. P. Flannery, *Numerical Recipes in C*, 2nd ed. (Cambridge University Press, Cambridge, 1992).

[32] F. Jensen, *Introduction to Computational Chemistry* (Wiley, Chicester, UK, 1999).

[33] W. F. van Gunsteren and H. J. C. Berendsen, *Gromos-87 Manual* (BIOMOS BV, Groningen, The Netherlands, 1987).

[34] A. R. van Buuren, S. J. Marrink, and H. J. C. Berendsen, J. Phys. Chem. **97**, 9206 (1993).

[35] A. E. Mark, S. P. van Helden, P. E. Janssen, and W. F. van Gunsteren, J. Am. Chem. Soc. **116**, 6293 (1994).

[36] H. J. C. Berendsen, D. van der Spoel, and R. van Drunen, Comput. Phys. Commun. **91**, 43 (1995).

[37] H. J. C. Berendsen, J. P. M. Postma, W. F. v. Gunsteren, A. DiNola, and J. R. Haak, J. Chem. Phys. **81**, 3684 (1984).

[38] M. P. Allen and D. J. Tildesley, *Computer Simulation of Liquids* (Oxford University Press, Oxford, 1987).

[39] A. J. Stone, *The Theory of Intermolecular Forces*, International Series of Monographs on Chemistry Vol. 32 (Oxford University Press, Oxford, 1996).

[40] J. P. Ryckaert, G. Ciccotti, and H. J. C. Berendsen, J. Comput. Phys. **23**, 327 (1977).

[41] B. Hess, H. Bekker, H. J. C. Berendsen, and J. G. E. M. Fraaije, J. Comput. Chem. **18**, 1463 (1997).

[42] H. J. C. Berendsen, J. R. Grigera, and T. P. Straatsma, J. Phys. Chem. **91**, 6269 (1987).

[43] K. Kwac, H. Lee, and M. Cho, J. Chem. Phys. **120**, 1477 (2004).

[44] E. Guardia, R. Pinzon, J. Casulleras, M. Orozco, and F. J. Luque, Mol. Simul. **26**, 287 (2001).

[45] W. L. Jorgensen, J. M. Briggs, and M. L. Contreras, J. Phys. Chem. **94**, 1683 (1990).

[46] T. l. C. Jansen, W. Zhuang, and S. Mukamel, J. Chem. Phys. **121**, 10577 (2004).

[47] S. Woutersen, Y. Mu, G. Stock, and P. Hamm, Chem. Phys. **266**, 137 (2001).

[48] O. Golonzka, M. Khalil, N. Demirdoven, and A. Tokmakoff, Phys. Rev. Lett. **86**, 2154 (2001).

[49] S. Mukamel, *Principles of Nonlinear Optical Spectroscopy* (Oxford University Press, New York, 1995).

[50] G. Eaton, M. C. R. Symons, and P. P. Rastogi, J. Chem. Soc., Faraday Trans. 1 **85**, 3257 (1989).

[51] D. W. Oxtoby, D. Levesque, and J.-J. Weis, J. Chem. Phys. **68**, 5528 (1978).

[52] C. P. Lawrence and J. L. Skinner, J. Chem. Phys. **117**, 8847 (2002).

[53] R. Rey and J. T. Hynes, J. Chem. Phys. **104**, 2356 (1996).

[54] S. J. V. Frankland and M. Maroncelli, J. Chem. Phys. **110**, 1687 (1999).